JACS
JOURNAL OF THE AMERICAN CHEMICAL SOCIETY
Article
pubs.acs.org/JACS

A New High-Energy Cathode for a Na-Ion Battery with Ultrahigh Stability

Young-Uk Park,[†,§,⊥] Dong-Hwa Seo,[†,‡,⊥] Hyung-Soon Kwon,[†] Byoungkook Kim,[∥] Jongsoon Kim,[†] Haegyeom Kim,[†] Inkyung Kim,[†,§] Han-Ill Yoo,[†] and Kisuk Kang*[,†,‡,§]

[†]Department of Materials Science and Engineering, [‡]Research Institute of Advanced Materials (RIAM), and [§]Center for Nanoparticle Research, Institute for Basic Science (IBS), Seoul National University, 1 Gwanak-ro, Gwanak-gu, Seoul 151-742, Korea

[∥]Research Analysis Center, KAIST, 291 Daehak-ro, Yuseong-gu, Daejeon 305-701, Korea

Supporting Information

ABSTRACT: Large-scale electric energy storage is a key enabler for the use of renewable energy. Recently, the room-temperature Na-ion battery has been rehighlighted as an alternative low-cost technology for this application. However, significant challenges such as energy density and long-term stability must be addressed. Herein, we introduce a novel cathode material, $Na_{1.5}VPO_{4.8}F_{0.7}$, for Na-ion batteries. This new material provides an energy density of ~600 Wh kg^{-1}, the highest value among cathodes, originating from both the multielectron redox reaction (1.2 e^- per formula unit) and the high potential (~3.8 V vs Na^+/Na) of the tailored vanadium redox couple ($V^{3.8+}/V^{5+}$). Furthermore, an outstanding cycle life (~95% capacity retention for 100 cycles and ~84% for extended 500 cycles) could be achieved, which we attribute to the small volume change (2.9%) upon cycling, the smallest volume change among known Na intercalation cathodes. The open crystal framework with two-dimensional Na diffusional pathways leads to low activation barriers for Na diffusion, enabling excellent rate capability. We believe that this new material can bring the low-cost room-temperature Na-ion battery a step closer to a sustainable large-scale energy storage system.

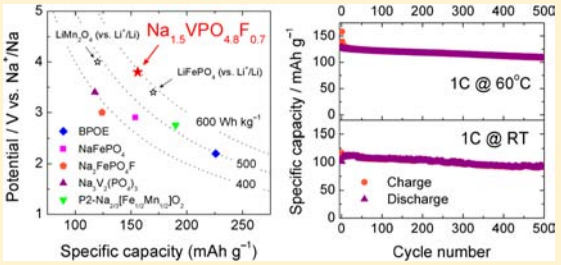

1. INTRODUCTION

Establishing a sustainable energy solution is one of the most important issues in efforts to achieve a sustainable society. Alternative energies such as solar, wind, and geothermal energy do not produce electricity coincident with consumption times. Thus, a large-scale energy storage system is essential to deal with such discrepancy. High-energy Li-ion batteries (LIBs) are expected to contribute in part to the solution; however, their high cost and low stability prohibit wide application in this area. Recently, attention has been refocused on room-temperature Na-ion batteries (NIBs) as a low-cost alternative technology as compared to LIBs.[1−7] The abundance and low cost of Na in the earth will become advantageous when a large amount of material is demanded for renewable energy solutions. Moreover, because rechargeable Na batteries share many similarities with LIBs, opportunities for fast-advancing NIB research can be found in state-of-the-art LIB technologies.

The classes and features of cathodes available for NIBs share common aspects with those of LIBs.[4−7] As the first successful Li battery cathode was layered oxides such as $LiCoO_2$, layered Na transition metal oxides have been studied extensively as NIB cathodes.[1,8−12] Recently, Komaba and co-workers succeeded in synthesizing P2-type layered $Na_x[Fe_{1/2}Mn_{1/2}]O_2$ as a new high-capacity cathode for NIBs, which showed the highest energy density (520 Wh kg^{-1}) of an NIB cathode to date.[1] Polyanion-based Na phases are also being explored as new cathode materials for NIBs. Various Na-intercalation materials have been suggested,[2,4−7,13−24] inspired by works on polyanion-based Li phases such as $LiFePO_4$ or earlier works on NASICONs (sodium super ionic conductors) such as $Na_3V_2(PO_4)_3$. More recently, unconventional approaches for NIB cathodes such as a bipolar porous organic electrode (BPOE) have been undertaken,[25,26] proposing a new possible NIB chemistry with a high energy density that can approach 500 Wh kg^{-1}.

Despite the current rigorous search for high-performance NIB electrode materials, their overall electrochemical performance remains inferior to Li chemistry. The less negative redox potential of Na^+/Na as compared to Li^+/Li (−2.71 and −3.04 V vs standard hydrogen electrode) reduces the operating voltage, leading to a generally lower energy density. The larger Na^+ ion as compared to the Li^+ ion (1.02 vs 0.59 Å) causes greater change in the host structure upon insertion or removal, which often results in poorer cycle life or even sluggish diffusion. Such fundamental demerits must be overcome to advance NIBs and their wide application as an alternative to LIBs.

In this study exploring a new NIB cathode, we attempted to counterbalance these limitations by searching for a material chemistry with a high redox potential and a rigid open framework that is less sensitive to the volume change from the

Received: June 15, 2013
Published: August 16, 2013

   dx.doi.org/10.1021/ja406016j | J. Am. Chem. Soc. 2013, 135, 13870−13878

guest ion insertion. In this regard, we focused on polyanion-based open crystal frameworks with vanadium redox couples. Recent studies have demonstrated that vanadium redox can exhibit high voltage in a Na cell. A relatively high average voltage of ~3.4 V (vs Na^+/Na) was achieved for $Na_3V_2(PO_4)_3$.[2,23] The V^{3+}/V^{4+} redox couple in $Na_3V_2(PO_4)_2F_3$ showed an even higher average voltage (~3.9 V) in a Na cell,[13] although its specific capacity remained limited due to the relatively heavy polyanion group. Moreover, we demonstrated that multielectron transfer of a vanadium redox couple is possible in certain polyanion frameworks maintaining its high potential. In our previous work,[27] we reported a new electrode, $Li_{1.1}Na_{0.4}VPO_{4.8}F_{0.7}$, for LIBs by tailoring the polyanion group of the crystal and expanded the redox range to $V^{3.8+}/V^{5+}$ in the high-voltage region. The tuned redox couple provided an additional 0.2 electrons per formula unit, as compared to the one electron transfer reaction of V^{4+}/V^{5+}.

Herein, we show that $Na_{1.5}VPO_{4.8}F_{0.7}$, the precursor of $Li_{1.1}Na_{0.4}VPO_{4.8}F_{0.7}$, can function as an excellent cathode for rechargeable Na batteries with a high energy density. It exceeds the state-of-the-art P2-type layered oxide with the highest energy density to date. Surprisingly, most electrochemical properties of this material such as its power capability and long-term cycle life outperform those of existing cathodes for NIBs and even rival those of LIB cathodes such as olivine $LiFePO_4$ and spinel $LiMn_2O_4$. The origin of the high battery performance is discussed through an analysis using combined theoretical and experimental tools.

2. EXPERIMENTAL SECTION

2.1. Synthesis. $Na_{1.5}VPO_{4.8}F_{0.7}$ and $Na_{1.5}VPO_5F_{0.5}$ powders were prepared by solid-state reaction using stoichiometric amounts of $VOPO_4$, VPO_4, NaF (Sigma-Aldrich, 99%), and Na_2CO_3 (Sigma-Aldrich, 99%) as precursor mixtures. Blending of the precursors was performed by high-energy ball-milling at 300 rpm for 24 h; the resulting mixtures were pelletized and sintered at 750 °C for 1.5 h under flowing argon. Detailed synthesis methods can be found in our previous report.[27] To obtain the $Na_{1.0}VPO_{4.8}F_{0.7}$ phase, Na^+ ions in the $Na_{1.5}VPO_{4.8}F_{0.7}$ powder were chemically extracted using a stoichiometric amount of NO_2BF_4 (Sigma-Aldrich, 95%) in acetonitrile solvent (Sigma-Aldrich) at room temperature. Following reaction for 6–15 h, the powder was washed, centrifuged several times with acetonitrile and ethanol, and then dried in a vacuum oven at 70 °C overnight. The atomic ratios of Na, V, and P were determined by inductively coupled plasma spectroscopy (Polyscan 60E; Thermo Jarrell Ash, U.S.).

2.2. SEM and TEM. Scanning electron microscopy (SEM) images were obtained using a SUPRA 55VP FE-SEM (Carl Zeiss, Germany) at an operating voltage of 2 kV. Transmission electron microscopy (TEM) images were acquired using a Tecnai F20 (FEI, U.S.) at an accelerating voltage of 200 kV.

2.3. XRD and XANES. Powder X-ray diffraction (XRD) patterns were recorded using an X-ray diffractometer (D8 Advance; Bruker, Germany) using Ni-filtered Cu Kα radiation (λ_1 = 1.54059 Å, λ_2 = 1.54431 Å) in the 2θ range of 10–60°. The room-temperature XRD data were refined with the space group of $P4_2/mnm$ using the Rietveld method and FullProf software.[28] X-ray absorption near-edge structure (XANES) spectra were recorded at room temperature at beamline 8C at the Pohang Accelerator Laboratory (PAL) in Korea using photons with a storage ring energy of 2.5 GeV and a current of 125 mA. They were collected in the transmission mode at the vanadium K-edge.

2.4. NMR Spectroscopy. Solid-state ^{31}P magic angle spinning (MAS) nuclear magnetic resonance (NMR) spectroscopy experiments were performed using an Agilent 400 MHz narrow bore spectrometer (1.6 mm probe) at a Larmor frequency of 161.98 MHz. A 90° pulse of 1.25 or 2.5 μs and recycle time of 0.1 s were used, and the shifts were referenced to 85% H_3PO_4 in aqueous solution (0 ppm). All experiments were conducted with a MAS frequency of 40 kHz at room temperature.

2.5. Electrochemical Characterization. A slurry of 70 wt % $Na_{1.5}VPO_{4.8}F_{0.7}$, 20 wt % carbon black, and 10 wt % polyvinylidene fluoride (PVDF, Sigma-Aldrich) dispersed in *N*-methyl-2-pyrrolidone (NMP, Sigma-Aldrich) was prepared and cast on aluminum foil. The electrode was dried at 120 °C, and the loading of the active material on the electrode was ca. 2–3 mg cm^{-2}. Electrochemical cells were assembled into CR2032-type coin cells in an Ar-filled glovebox (MBraun, Germany). Na metal (Sigma-Aldrich) and a glass microfiber filter (grade GF/F; Whatman, U.S.) were used as a counter electrode and separator, respectively. Unless otherwise noted, 1 M $NaClO_4$ in propylene carbonate (PC, Sigma-Aldrich) was used as an electrolyte, and all electrochemical tests were performed at room temperature using a potentiostat/galvanostat (WBCS 3000; WonA Tech, Korea). To prepare the $Na_xVPO_{4.8}F_{0.7}$ electrodes for the ex situ XRD experiment, the electrochemical cells were galvanostatically charged or discharged at a *C*/10 rate and disassembled at various states of charge and depths of discharge. Prior to XRD experiments, the electrodes were washed with PC and dried overnight in a vacuum oven at 70 °C. On the basis of one electron transfer, 1*C* was calculated to correspond to 129.7 mA g^{-1}.

For galvanostatic intermittent titration technique (GITT) measurement, the electrochemical cells were rested for 2 h after each hour-long charging or discharging at a *C*/10 rate. Combined GITT and electrochemical impedance spectroscopy (EIS) measurement was carried out for the first charge process. An electrochemical cell comprising the $Na_{1.5}VPO_{4.8}F_{0.7}$ cathode was charged for 11 min in galvanostatic mode at a *C*/5 rate and rested for 1 h. EIS spectra were recorded at the end of each rest step between 1 MHz and 1 Hz, with a sinus amplitude of 10 mV. This sequence was repeated when the operating voltage reached 4.5 V (vs Na^+/Na) using a multichannel potentiostat/galvanostat with EIS (VSP-300; Bio-Logic, France). For the room-temperature rate capability test, the $Na_{1.5}VPO_{4.8}F_{0.7}$ powder was subjected to a dry carbon-coating process; 20 wt % carbon black was blended, and the mixture was ball-milled for 24 h. In this test, the total active content in the electrode was 72 wt %, and the voltage window was 1.5–4.6 V (vs Na^+/Na).

2.6. Electrical Conductivity (ac) Measurements. The $Na_{1.5}VPO_{4.8}F_{0.7}$ and $Na_{1.0}VPO_{4.8}F_{0.7}$ powders were pressed into pellets with 15 mm diameters and ~1 mm thicknesses using a uniaxial press (400 kg cm^{-2}). They were further compacted at 200 MPa for 6 min by cold isostatic press; a compactness of ~70% of the pellet was obtained without sintering. The 50 nm-thick platinum layers were deposited on both sides of the pellets by sputtering. The bulk conductivities of the pellets were measured using two-probe ac impedance spectroscopy (models 1260 and 1296; Solatron, UK) and the ZView electrochemical impedance software (Scribner Associates, U.S.). EIS data were recorded from 1 MHz to 100 mHz with a voltage perturbation of 1 V. Bulk conductivities (ac) were calculated from both the geometries of the pellets and the bulk resistance values, which were obtained by one-circle fitting of the high-frequency region in the EIS spectra. Finally, activation energies (ac) were obtained using linear interpolation of the conductivity values at various temperatures by the Arrhenius equation: $\sigma T = \sigma_0 \exp(-E_a/k_BT)$, where σ is conductivity, T is temperature, E_a is activation energy, and k_B is the Boltzmann constant. Room-temperature conductivities were estimated by linear extrapolation of the measured data points.

2.7. Computational Details. First-principle calculations were performed using the Perdew–Burke–Ernzerhof exchange-correlation parametrization to density functional theory (DFT) with the spin-polarized generalized gradient approximation (GGA).[29] We used a plane-wave basis set and the projector-augmented wave (PAW) method as implemented in the Vienna ab initio simulation package (VASP).[30] Hubbard parameters (GGA+*U*)[31] were added to correct the incomplete cancellation of the self-interaction of GGA. A *U* value of 5.0 eV (the on-site Coulomb term) and *J* value of 1.0 eV (the exchange term) were used for the vanadium ions.[13] To study $Na_xVPO_5F_{0.5}$ phases, we considered all possible Na-vacancy orderings

dx.doi.org/10.1021/ja406016j | J. Am. Chem. Soc. 2013, 135, 13870–13878

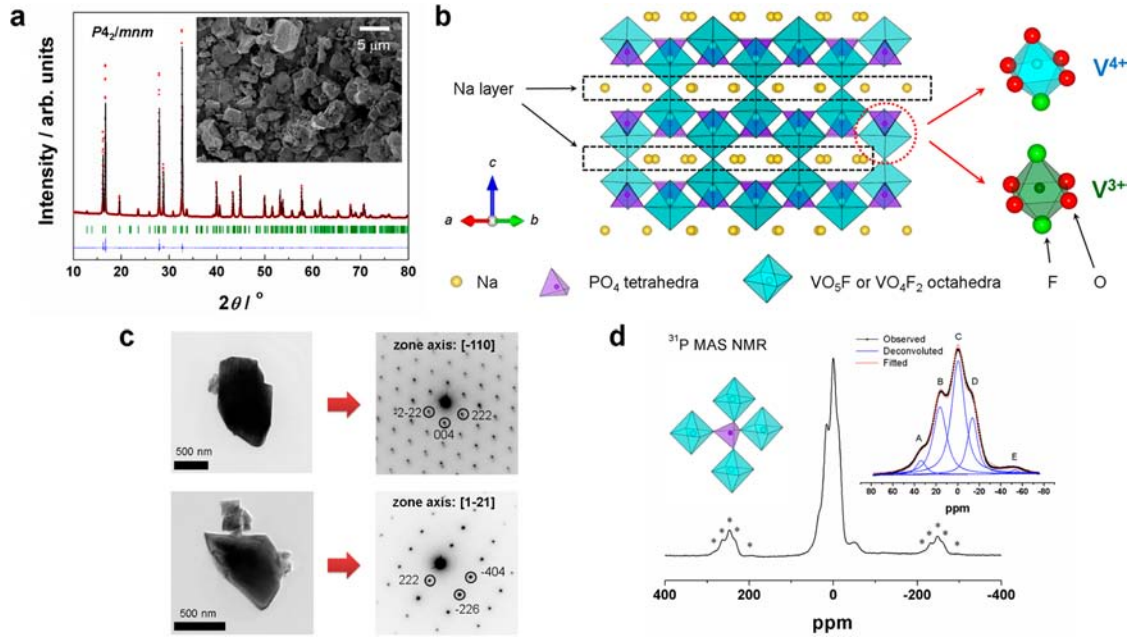

Figure 1. (a) Powder XRD pattern of $Na_{1.5}VPO_{4.8}F_{0.7}$ and its Rietveld refinement with observed data points (red dots), calculated pattern (black line), difference curve (blue line), and Bragg positions (green bars); lattice parameters in the space group of $P4_2/mnm$ were $a = b = 9.03057(9)$ Å, $c = 10.6282(1)$ Å, and $V = 866.74(2)$ Å^3. The inset shows an SEM image (magnification: ×5000). (b) Crystal structure of $Na_{1.5}VPO_{4.8}F_{0.7}$ and two different local environments for V^{4+} and V^{3+} ions (i.e., VO_5F and VO_4F_2 octahedra, respectively). The Na, V, P, O, and F atoms are depicted as yellow, cyan, purple, red, and green spheres, respectively. The Na layers are denoted as dashed boxes. (c) Bright-field TEM images of $Na_{1.5}VPO_{4.8}F_{0.7}$ particles (left) and the corresponding SAED patterns (right); most particles were single-crystalline, as only spot patterns were observed. (d) ^{31}P MAS NMR spectrum of $Na_{1.5}VPO_{4.8}F_{0.7}$. Spinning sidebands are marked with asterisks. At least five isotropic shifts exist around 0 ppm (right inset). The left inset shows a schematic representation of the local environment of a PO_4 tetrahedron. One PO_4 tetrahedron is affected by four adjacent vanadium ions via the Fermi-contact interaction.

within the unit cell of $Na_xVPO_5F_{0.5}$ ($0.5 \le x \le 1.5$) generated with the CASM program.[32,33] Among them, we picked up 30 Na-vacancy orderings with the lowest electrostatic energy at each composition through the Ewald summation method[34] and then calculated their energies with GGA+U. We determined a voltage profile of $Na_xVPO_5F_{0.5}$ in a Na cell using following equation: $\langle V \rangle = -[E(Na_{x1}VPO_5F_{0.5}) - E(Na_{x2}VPO_5F_{0.5}) - (x_1 - x_2) \times E(Na)]/[(x_1 - x_2) \times F]$, where E is the DFT energy of the most stable structure and F is the Faraday constant.

Activation energies for Na vacancy diffusion in $Na_xVPO_5F_{0.5}$ ($x \approx 1.5$ and 0.5) were calculated using the nudged-elastic-band (NEB) method.[35] In these calculations, the Na^+ ions were allowed to move in the unit cell of $Na_{23/16}VPO_5F_{0.5}$. Five or seven replicate systems were used as the starting points for the NEB method, with linear interpolation between the initial and final states of the plausible diffusion pathways. All lattice parameters were fixed at the $Na_{1.5}VPO_5F_{0.5}$ states, but all internal degrees of freedom were relaxed during the NEB calculations. The bond valence mismatch map was calculated using the 3DBVSMAPPER program[36] and drawn using the VESTA program.[37]

3. RESULTS

3.1. Material Characterization of $Na_{1.5}VPO_{4.8}F_{0.7}$. Phase-pure $Na_{1.5}VPO_{4.8}F_{0.7}$ with no notable impurity was obtained successfully (Figure 1a). The composition and oxidation state of vanadium ions of $Na_{1.5}V^{3.8+}PO_{4.8}F_{0.7}$ were confirmed by multiple lines of evidence in the previous report.[27] The fluorine-substituted $Na_{1.5}VPO_{4.8}F_{0.7}$ phase was isostructural to both $Na_{1.5}VPO_5F_{0.5}$ and $Na_3V_2(PO_4)_2F_3$ (or $Na_{1.5}VPO_4F_{1.5}$), with a space group of $P4_2/mnm$.[27] Refinement of the crystal structure of $Na_{1.5}VPO_{4.8}F_{0.7}$ indicated that the corner-sharing between PO_4 tetrahedral and VO_5F/VO_4F_2 octahedral units constructs a three-dimensional open framework where Na^+ ions can be inserted into the interstitial sites (Figure 1b). The overall crystal framework can also be described as a pseudolayered structure because the intercalant Na^+ ions form Na layers on the ab plane in the structure. The sizes of $Na_{1.5}VPO_{4.8}F_{0.7}$ particles ranged from 1 to 5 μm (Figure 1a, inset), and each particle was composed of a single crystalline domain, as shown by transmission electron microscopy (TEM) and selected-area electron diffraction (SAED) in Figure 1c.

As a result of fluorination, two types of vanadium local environment, VO_5F and VO_4F_2 octahedra, were generated. This also led to the mixed valence state of vanadium (i.e., coexistence of V^{4+} and V^{3+} ions) in $Na_{1.5}VPO_{4.8}F_{0.7}$, which was confirmed previously by the double titration method and electron paramagnetic resonance (EPR) experiments.[27] Generally, NMR can provide clear evidence for the mixed valence states of transition metals by quantitatively showing the distribution of the paramagnetic entities.[38,39] The distribution of V^{4+} and V^{3+} ions in $Na_{1.5}VPO_{4.8}F_{0.7}$ was probed by ^{31}P MAS NMR measurements (Figure 1d). Each P atom is affected by four adjacent V^{n+} ions via Fermi-contact interaction (Figure 1d, inset). As the two valence states of vanadium (V^{4+} and V^{3+} ions) have dissimilar strengths of paramagnetism in the structure, various local environments can be created by different distributions of V^{4+} and V^{3+} ions around P atoms (see Supporting Information Figure S1c for all possible combinations). This causes the diversity in Fermi-contact shifts in ^{31}P MAS NMR spectra, in contrast to cases with one valence state of vanadium ions in the material, where only two types of local environment exist for P atoms. For example, the ^{31}P MAS NMR spectrum of $Na_{1.5}VPO_{4.8}F_{0.7}$ shows at least four major isotropic shifts (Figure 1d), whereas $Na_{1.5}VPO_5F_{0.5}$ shows only

dx.doi.org/10.1021/ja406016j | J. Am. Chem. Soc. 2013, 135, 13870−13878

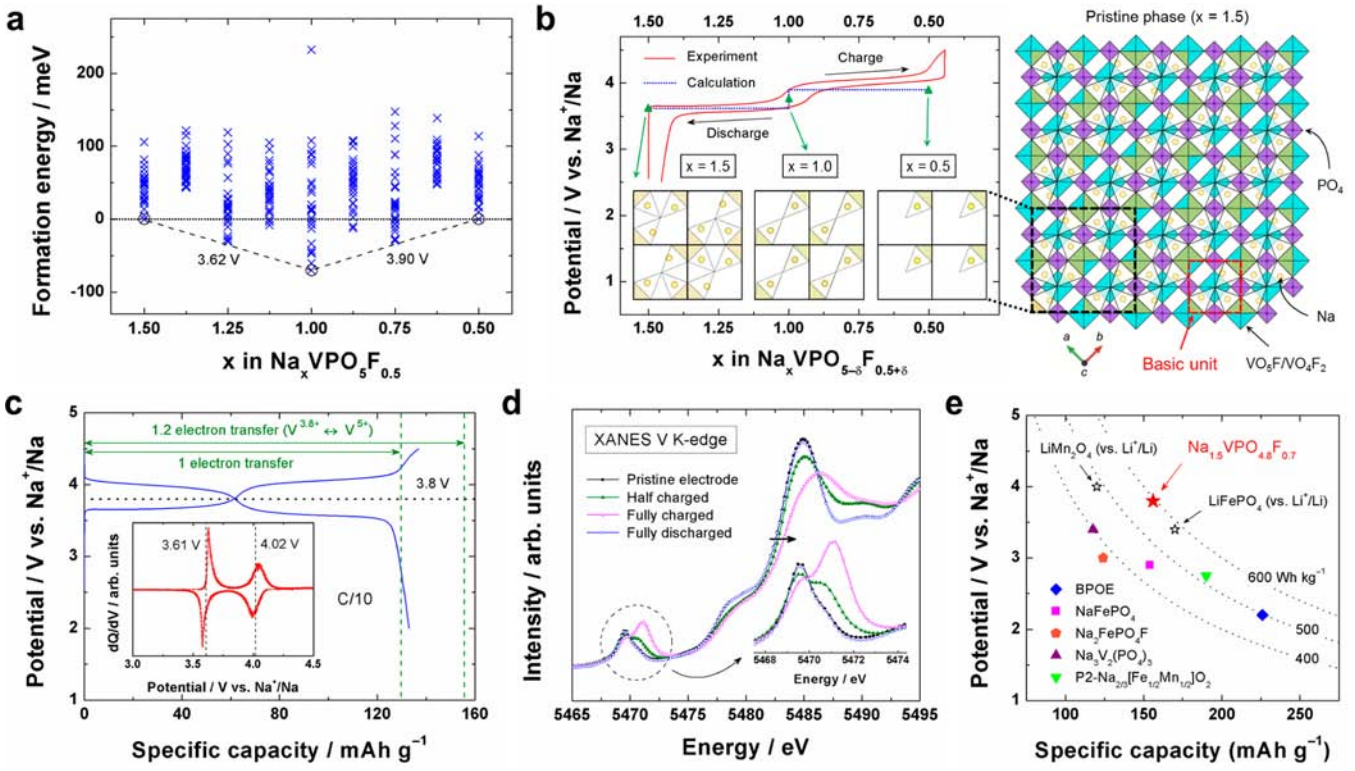

Figure 2. (a) Formation energy plot of $Na_xVPO_5F_{0.5}$ from first-principle calculations. (b) Comparison of voltage versus composition curves from experiments (red solid line) and calculations (blue dotted line). The inset shows the most stable Na-vacancy configuration in the Na layer (on the *ab* plane) for each Na content (x = 1.5, 1.0, and 0.5) in the calculations. Complete crystal structure on the *ab* plane of the pristine phase (x = 1.5) is shown on the right side, where a basic unit (i.e., the smallest unit for defining the Na-vacancy ordering in the Na layer) is denoted as a red dashed box. The number of Na^+ ions per basic unit (n) is a fingerprint of each phase; n = 3, 2, and 1 for x = 1.5, 1.0, and 0.5, respectively. Note that no mixture of n = 3 and 1 occurred in the intermediate phase (x = 1.0). (c) Charge/discharge profile at a $C/10$ rate for the $Na_{1.5}VPO_{4.8}F_{0.7}$ cathode (voltage window: 2.0−4.5 V vs Na^+/Na). The average voltage (3.8 V vs Na^+/Na) is represented as a horizontal dotted line. The capacities based on 1 electron transfer (129.7 mAh g^{-1}) and 1.2 electron transfer (155.6 mAh g^{-1}) are shown as vertical dashed lines, respectively. The 1C rate corresponds to 129.7 mA g^{-1}. The inset shows the corresponding dQ/dV curve. (d) Vanadium K-edge XANES spectra of the $Na_xVPO_{4.8}F_{0.7}$ electrodes with different states of charge or depths of discharge. The inset shows an enlarged graph of the pre-edge region. (e) Energy density comparison of various cathode materials for NIBs and LIBs.

two (Supporting Information Figure S1a); this difference provides consistent evidence for the mixed valence state of vanadium in $Na_{1.5}VPO_{4.8}F_{0.7}$. A detailed explanation is provided in the Supporting Information, including Figure S1 and Table S1.

3.2. Electrochemical Properties of $Na_{1.5}VPO_{4.8}F_{0.7}$. Prior to electrochemical tests in Na batteries, the Na extraction behavior of $Na_{1.5}VPO_{4.8}F_{0.7}$ was monitored via first-principle calculations on a simpler isostructural $Na_{1.5}VPO_5F_{0.5}$ system. Figure 2a shows the calculated formation energies of $Na_xVPO_5F_{0.5}$ with various Na-vacancy configurations for selected Na contents. The energy plot shows a minimum at x = 1.0, implying the strong tendency for a stable intermediate phase at this composition. The existence of the intermediate phase at this composition was identified by ex situ XRD study, which will be discussed later. Generally, intermediate phases are often observed in Na-intercalation compounds.[8,40] Na^+−Na^+ electrostatic repulsion, as well as the interaction between Na^+ and transition metal ions, leads to strong Na-vacancy ordering at certain Na concentrations, forming a stable intermediate phase, as recently demonstrated for P2-Na_xCoO_2.[8,40] Similarly, the intermediate phase (at x = 1.0) in our $Na_xVPO_{5-\delta}F_{0.5+\delta}$ ($0 \le \delta \le 0.2$) system likely originated from Na-vacancy ordering.

First-principle calculations suggested the most energetically plausible Na-vacancy configurations in the stable phases of $Na_xVPO_{5-\delta}F_{0.5+\delta}$ (x = 1.5, 1.0, and 0.5; Figure 2b, inset). The as-prepared material (x = 1.5) contained three Na^+ ions per basic unit of the Na layer (indicated in a red box in Figure 2b, right panel), while there are four crystallographically equivalent Na sites per basic unit. Each basic unit contained the same number (three) of Na^+ ions, without segregation into two and four Na^+ ion occupations in two basic units, which we attribute to Na^+−Na^+ repulsion inside the basic units of the Na layers. Because of the strong Na^+−Na^+ repulsion, Na^+ ions do not occupy the centers of the interstitial sites, but have shifted positions. When 0.5 Na^+ ions were extracted from the material, the repulsive force could be greatly relieved by Na-vacancy reordering through the diagonal configuration (x = 1.0; Figure 2b, inset). This change accompanied the increased symmetry of the intermediate phase. Indeed, we later observed in the experimental structure characterization that $Na_{1.0}VPO_{4.8}F_{0.7}$ transformed from $P4_2/mnm$ to the higher-symmetry space group of $I4/mmm$ (see Supporting Information Figure S2 for details). The diagonal Na-vacancy configuration that minimizes electrostatic repulsion is believed to further stabilize the $Na_{1.0}VPO_5F_{0.5}$ intermediate phase as compared to the mixture of two-end members (i.e., $Na_{1.5}VPO_5F_{0.5}$ and $Na_{0.5}VPO_5F_{0.5}$). The large stabilization of the intermediate phase by both one Na extraction per basic unit (n = 3 → 2) and the diagonal Na-vacancy configuration causes a voltage gap at the composition

dx.doi.org/10.1021/ja406016j | J. Am. Chem. Soc. 2013, 135, 13870−13878

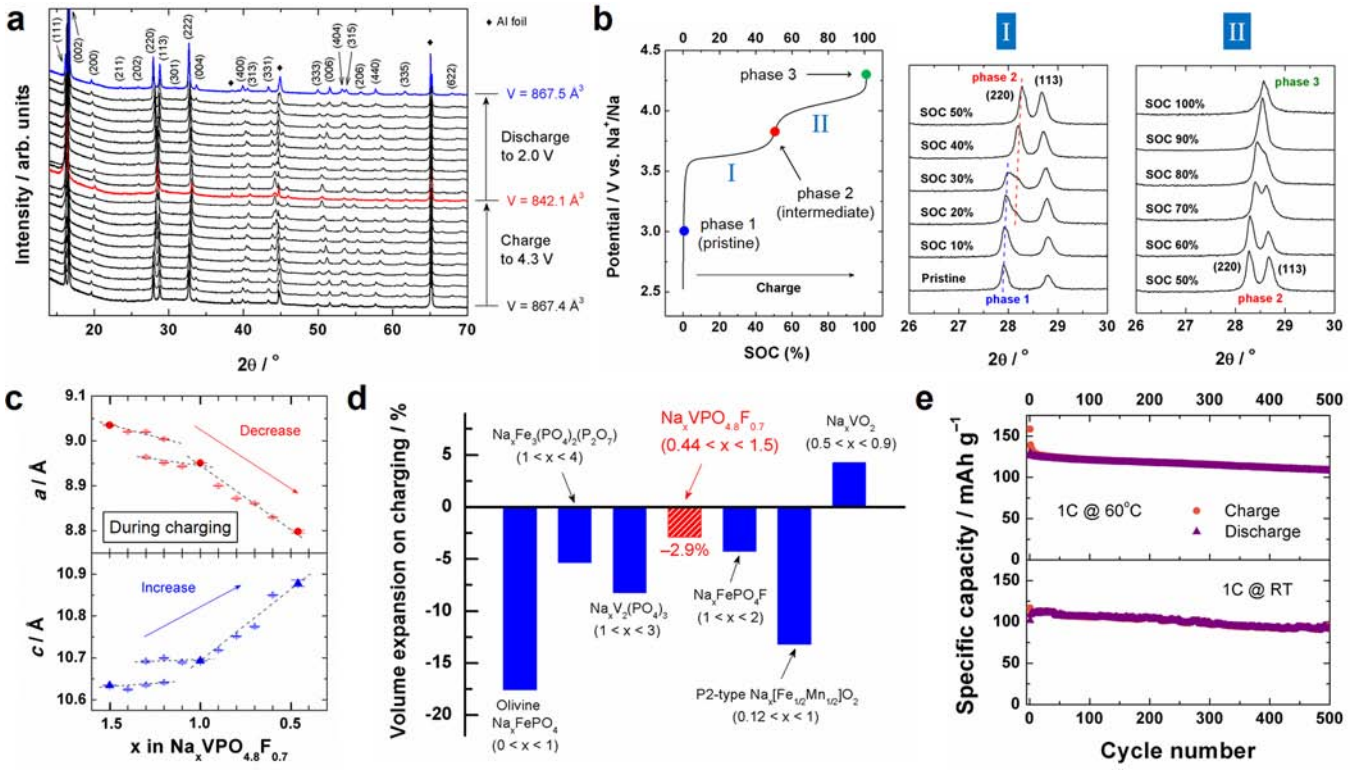

Figure 3. (a) Ex situ XRD patterns of the $Na_xVPO_{4.8}F_{0.7}$ electrodes with different states of charge (SOCs) and depths of discharge (DODs). The intervals were identical (10%). The XRD patterns of the fully charged state (at 4.3 V vs Na^+/Na) and the fully discharged state (at 2.0 V vs Na^+/Na) were denoted as red and blue colors, respectively. The refined unit cell volumes of the pristine, fully charged, and fully discharged phases were 867.4, 842.1, and 867.5 $Å^3$, respectively. The Rietveld refinements and the indexing of the reflections were based on the space group of $P4_2/mnm$. Peaks marked with diamonds are from aluminum foil in the electrodes. (b) Evolution of (220) and (113) reflections of the ex situ XRD patterns at different SOCs in regions I and II during charging (right figures). The left panel shows a typical voltage profile of the $Na_{1.5}VPO_{4.8}F_{0.7}$ electrode as a function of SOC; regions I and II correspond to the low-voltage and high-voltage regions, respectively. Phases 1 (blue), 2 (red), and 3 (green) represent the pristine phase ($Na_{1.5}VPO_{4.8}F_{0.7}$), the intermediate phase ($Na_{1.0}VPO_{4.8}F_{0.7}$), and the fully charged phase, respectively. (c) Changes in lattice parameters a and c with Na content (x) in the $Na_xVPO_{4.8}F_{0.7}$ electrodes during charging. (d) Comparison of volume changes on charging in various cathodes for NIBs. (e) Cycle life of the $Na_{1.5}VPO_{4.8}F_{0.7}$ electrode at room (25 °C; bottom) and high (60 °C; top) temperatures. The electrochemical cells were cycled at a 1C rate with a voltage window of 2.0−4.7 V using the electrolyte of 1 M $NaBF_4$ in a mixture of ethyl carbonate and propylene carbonate (1:1 v/v). We believe that the capacity fading for the first few charge cycles at 60 °C (top) is due to the decomposition of the electrolyte at both high voltage and elevated temperature.

of x = 1.0 (Figure 2b, blue profile), which is in good agreement with the experiment, as indicated by the red profile in Figure 2b. The calculated operating voltages for two regions (3.62 and 3.90 V) yielded an average voltage of 3.76 V (vs Na^+/Na), which was also comparable to the experimental value (Figure 2b, red profile) of ∼3.8 V measured in a Na half-cell using a Na metal anode. The average voltage of $Na_{1.5}VPO_{4.8}F_{0.7}$ (∼3.8 V vs Na^+/Na) is an impressively high value for a cathode material for NIBs. The high voltage of $Na_{1.5}VPO_{4.8}F_{0.7}$ electrode can be attributed to the high redox potential of the vanadium couple, aided by the large inductive effect of the fluorophosphate group.[41]

Galvanostatic measurement at a $C/10$ rate revealed that the specific capacity could be enhanced via the multielectron redox reaction of vanadium ($V^{3.8+} \leftrightarrow V^{5+}$) in a Na cell (Figure 2c). The discharge capacity (∼134 mAh g^{-1}) at a $C/10$ rate simply exceeded the theoretical capacity (129.7 mAh g^{-1}), based on one electron transfer for both charging and discharging, which is consistent with our observations for $Li_{1.1}Na_{0.4}VPO_{4.8}F_{0.7}$.[27] It should be noted that the additional V^{3+}/V^{4+} redox reaction from the widened redox range in $Na_{1.5}V^{3.8+}PO_{4.8}F_{0.7}$ does not exhibit voltage well below that of V^{4+}/V^{5+}, but is rather comparable to the V^{3+}/V^{4+} redox potential of ∼3.9 V (vs Na^+/Na) in $Na_3V_2(PO_4)_2F_3$.[13] For $Na_{1.5}VPO_{4.8}F_{0.7}$, the additional fluorination that induces V^{3+} formation is considered to create a local environment of $V^{3+}O_4F_2$ similar to $Na_3V_2(PO_4)_2F_3$, sustaining the reasonably high voltage for the V^{3+}/V^{4+} redox reaction. Cycling at a $C/10$ rate showed two peaks at 3.61 and 4.02 V (vs Na^+/Na) in the dQ/dV curve (Figure 2c, inset), implying two different reactions, which will be discussed later.

The evolution of the vanadium oxidation state in $Na_xVPO_{4.8}F_{0.7}$ electrodes could be clearly identified by XANES analysis of the vanadium K-edge during charging and discharging process (Figure 2d). During charging, the edge of the spectrum shifted toward a higher energy, indicating oxidation of the vanadium ion. During the reverse reaction, it completely returned to the initial state, implying that the vanadium redox reaction is fully reversible. A clearer change was observed in the pre-edge region, where the pre-edge peak reversibly arose at a higher energy region during cycling, which is consistent with previous reports.[42,43]

On the basis of the average voltage of 3.8 V (vs Na^+/Na), the theoretical energy density of the $Na_{1.5}VPO_{4.8}F_{0.7}$ cathode can reach 600 Wh kg^{-1} (3.8 V × 155.6 mAh g^{-1} = 591.3 Wh kg^{-1}), assuming 1.2 electrons are supplied (155.6 mAh g^{-1}) from the $V^{3.8+}/V^{5+}$ redox couple. We emphasize that the $Na_{1.5}VPO_{4.8}F_{0.7}$

dx.doi.org/10.1021/ja406016j | J. Am. Chem. Soc. 2013, 135, 13870−13878

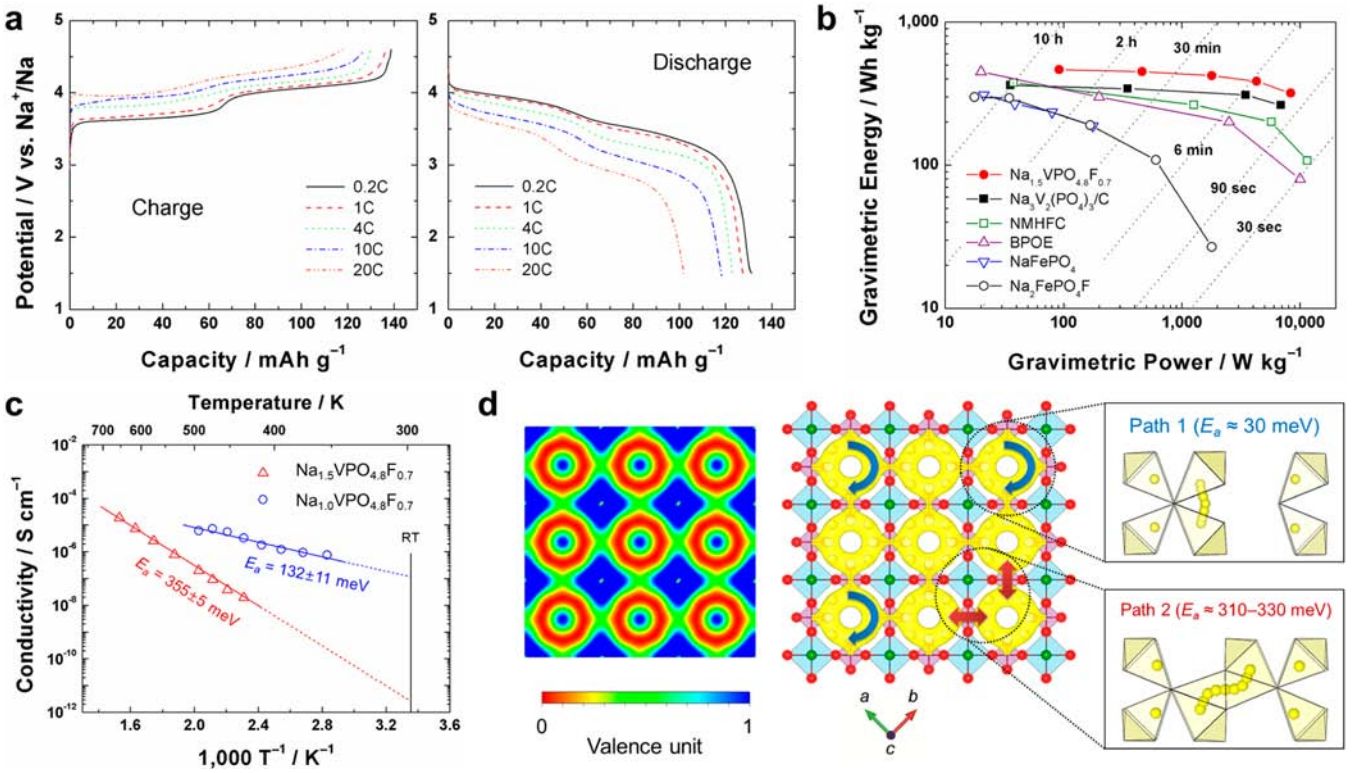

Figure 4. (a) Charge (left) and discharge (right) profiles of the $Na_{1.5}VPO_{4.8}F_{0.7}$ cathode at various *C* rates. (b) Ragone plot for the $Na_{1.5}VPO_{4.8}F_{0.7}$ cathode and other cathode materials for NIBs. (c) Arrhenius plot of electrical conductivities of $Na_{1.5}VPO_{4.8}F_{0.7}$ (red triangles) and $Na_{1.0}VPO_{4.8}F_{0.7}$ (blue circles) pellets at various temperatures. Activation energies (E_a) were calculated from the slopes of the fitted lines. E_a for the former and the latter were 355 ± 5 and 132 ± 11 meV, respectively. Room-temperature (RT) conductivities were estimated by linear extrapolation of the measured data points. (d) Bond valence mismatch map for Na in the $Na_{1.5}VPO_{5-\delta}F_{0.5+\delta}$ crystal structure (left). The spatial distribution of the bond valence mismatch on the *ab* plane is represented. The colors represent bond valence mismatches ranging from 0 (red) to 1 (blue). Yellow isosurfaces (isovalue = ±0.45 valence unit) represent the possible two-dimensional Na diffusional pathways on the *ab* plane (right figures). Enlarged figures show the trajectories and activation barriers for Na hopping for path 1 (blue arrows) and path 2 in $Na_xVPO_5F_{0.5}$ (red arrows).

cathode exhibits the highest energy density among cathode materials for NIBs (Figure 2e). The energy densities of polyanion-based cathodes such as $NaFePO_4$, Na_2FePO_4F, and $Na_3V_2(PO_4)_3$ hover around 400 Wh kg^{-1}, and only a few cathode materials such as the P2-type $Na_x[Fe_{1/2}Mn_{1/2}]O_2$ and BPOE have been reported to have energy densities approaching 500 Wh kg^{-1}.[1,2,16,17,20−26] The energy density of the $Na_{1.5}VPO_{4.8}F_{0.7}$ cathode (~600 Wh kg^{-1}) holds a unique position among cathode materials for NIBs with a high operating voltage. Moreover, it can rival state-of-the-art LIB cathode materials such as $LiFePO_4$ (theoretical energy density of 580 Wh kg^{-1}) and $LiMn_2O_4$ (480 Wh kg^{-1}), indicating the promise of its application as an alternative chemistry to LIB.

3.3. Structural Evolution of the $Na_xVPO_{4.8}F_{0.7}$ Electrode upon Cycling. To understand the charge/discharge mechanism of the $Na_xVPO_{4.8}F_{0.7}$ electrode in Na batteries, ex situ XRD experiments were carried out (Figure 3a−c; see Supporting Information Figure S3 for more complete pictures). Overall, a continuous peak shift was observed, implying a widespread solid−solution region. However, closer examination of the ex situ XRD patterns in Figure 3b revealed that two phases coexisted in the first half of the charge (i.e., region I), indicating the existence of the stable intermediate phase at x = 1.0. Conversely, signs of a biphasic reaction were difficult to identify in region II, implying a widespread miscibility gap. After a cycle, the XRD pattern returned to the pristine state, suggesting structural reversibility. Figure 3c shows the changes in lattice parameters of $Na_xVPO_{4.8}F_{0.7}$ phases during charging: a continuous decrease in lattice parameter a and increase in lattice parameter c with decreasing Na content. The reduction of lattice parameter a is attributed to the contraction of vanadium octahedra with the oxidation of V^{n+} ions. On the other hand, lattice parameter c increased due to the developing electrostatic repulsion between O^{2-} layers, as the Na layers that screen the electrostatic repulsion between O^{2-} layers became empty with charging. Interestingly, the same tendency is typically observed in layered oxides such as Na_xCoO_2 and Li_xCoO_2, which reminds that the $Na_{1.5}VPO_{4.8}F_{0.7}$ crystal can be described as a pseudolayered structure. The discussion on the charge/discharge mechanism of the $Na_xVPO_{4.8}F_{0.7}$ electrode will be continued in the Discussion.

The opposite trends of the two lattices with desodiation/sodiation of the $Na_xVPO_{4.8}F_{0.7}$ electrode were three-dimensionally counterbalanced, resulting in a surprisingly small volume change upon cycling (2.9%; $0.44 \le x \le 1.5$). Usually, Na^+ ion intercalation accompanies a large volumetric change due to the larger ionic size of the Na^+ ion as compared to the Li^+ ion, which often leads to limited cycle stability and practical capacity.[1,9,11,12] However, $Na_{1.5}VPO_{4.8}F_{0.7}$ undergoes one of the smallest volume changes with full charge/discharge among cathode materials for NIBs (Figure 3d).[1,2,10,16,17,24,44] The 2.9% volume change is comparable to that predicted from the first-principle calculations (ΔV = 3.1%) in our previous work.[27] The exceptionally small volume change gives rise to excellent

dx.doi.org/10.1021/ja406016j | J. Am. Chem. Soc. 2013, 135, 13870−13878

cyclability of the $Na_{1.5}VPO_{4.8}F_{0.7}$ cathode at room and high (60 °C) temperatures (Figure 3e). 95% of the initial capacity was retained after 100 cycles. Furthermore, more than 83% and 84% of the initial capacity were maintained after extended 500 cycles at room and high temperatures, respectively. We believe that this outstanding cycle life is due to the small volume change of the rigid polyanion framework that is less sensitive to Na insertion/extraction. Even after 515 cycles, we found no trace of structural deterioration in the electrode, implying a remarkably stable charge/discharge process (Supporting Information Figure S4). The correlation between the small volume change and stable cycle property is reminiscent of the well-known zero-strain $Li_4Ti_5O_{12}$ electrode for LIBs, indicating the importance of the small volume change in achieving high cycle stability.[45] We also found that after ~300 cycles, the electrode recovered most of the initial capacity when reassembled into another electrochemical cell using new Na metal foil and fresh electrolyte (Supporting Information Figure S5). This result indicates that the observed capacity fading is mainly due to the oxidation of Na metal or the decomposition of the electrolyte during cycling, rather than the degradation of the material.

3.4. Kinetics of the $Na_xVPO_{4.8}F_{0.7}$ Electrode. The kinetic behavior of the $Na_{1.5}VPO_{4.8}F_{0.7}$ electrode was first examined using the galvanostatic intermittent titration technique. The negligible overpotential values (~20 mV) throughout the whole charge/discharge process implied potentially fast kinetics of the electrode (Supporting Information Figure S6). In effect, high power capabilities during charging and discharging were observed in the rate tests of the $Na_{1.5}VPO_{4.8}F_{0.7}$ electrode in the Na cell (Figure 4a). From 0.2*C* to 1*C*, only negligible capacity reduction was detected with a remarkably small polarization. Even at the 20*C* rate, the charge/discharge exhibited reasonably small polarization with a high capacity. A capacity more than 100 mAh g^{-1} could be delivered at a 3 min charge/discharge rate (20*C* rate). Notably, the particle sizes of $Na_{1.5}VPO_{4.8}F_{0.7}$ ranged from 1 to 5 μm with no special treatment. This result is in contrast to conventional polyanion-based cathodes such as $Na_3V_2(PO_4)_3$ and $LiFePO_4$, which must be fabricated with nanomorphology with proper conductive coatings to achieve a high power capability. The Ragone plot in Figure 4b depicts the trade-off between energy and power density of the $Na_{1.5}VPO_{4.8}F_{0.7}$ electrode in comparison with the performance of various state-of-the-art NIB electrodes whose power capabilities have been reported. According to the plot, the $Na_{1.5}VPO_{4.8}F_{0.7}$ electrode showed the highest energy density throughout a wide range of charge and discharge rates.[20,22,23,25,46]

Despite this high power capability, EIS experiments revealed a relatively low electrical conductivity of pristine $Na_{1.5}VPO_{4.8}F_{0.7}$ (~2.4×10^{-12} S cm^{-1} at room temperature; Figure 4c). However, the low activation energy (E_a) of ~350 meV hinted at its fast kinetics (see Supporting Information Figure S7 for the EIS spectra at various temperatures), which is lower than those of other polyanion-based cathodes for LIBs such as $LiFePO_4$ (~600 meV)[47] and $LiFeSO_4F$ (~990 meV).[48] Interestingly, we found that electrical conductivity increased dramatically, by 5 orders of magnitude, in the $Na_{1.0}VPO_{4.8}F_{0.7}$ phase (~1.2×10^{-7} S cm^{-1} at room temperature; Figure 4c). As compared to room-temperature electrical conductivities of other polyanion-based LIB cathodes such as $LiFePO_4$ (~10^{-9} S cm^{-1})[47] and $LiFeSO_4F$ (~10^{-11} S cm^{-1}),[48] the conductivity of ~10^{-7} S cm^{-1} is much higher. More interestingly, its E_a (~130 meV) was remarkably low and far less than that of the NASICON-type $Na_3Zr_2Si_2PO_{12}$ (~330 meV) and most Na^+ ion-conducting solid electrolytes.[49,50] The substantial increase in conductivity upon the change of guest ion concentration is reminiscent of the behavior of $Li_4Ti_5O_{12}$, which is an insulator in the pristine state but becomes conductive, exhibiting very high power capability.[51] Because the conductive intermediate phase, $Na_{1.0}VPO_{4.8}F_{0.7}$, is related to the phase reactions of all regions (Supporting Information Figure S3), a fast electrode reaction is believed to be possible except for in the very initial state. Indeed, we observed rapidly improved kinetics of the charge transfer reaction with decreasing Na content of the $Na_xVPO_{4.8}F_{0.7}$ cathode in successive EIS measurements (see Supporting Information Figure S8 for the evolution of EIS spectra).

The first-principle calculations indicated that the rapid Na ionic diffusion is possible in the *ab* plane with low activation barriers for $Na_xVPO_5F_{0.5}$. Figure 4d shows that two Na diffusion paths exist in the *ab* plane. The activation barrier for path 1 was about 30 meV,[27] and that for path 2 was 310−330 meV (see Supporting Information Figure S9 for the activation energy curves for path 2 for $x \approx 1.5$ and 0.5). This indicates that path 2 is a rate-determining step for the successive diffusion of Na^+ ions in the bulk, while path 1 provides ultrafast hopping of Na, even at room temperature. The activation barrier of ~300 meV is comparable with those of layered Li transition metal oxide cathodes for LIBs, including $LiNiO_2$ and $LiCoO_2$.[52] This result indicates that Na diffusion in the electrode for NIBs is not necessarily slow, despite its larger ionic size, and it is more dominantly affected by its host crystal structure. The two-dimensional nature of Na diffusion can also be beneficial for high power. In a one-dimensional diffuser such as $LiFePO_4$, Li migration can be sensitively retarded by small amounts of defects; thus, a large particle size that can contain defects with higher probability is not suitable.[53] In contrast, the $Na_{1.5}VPO_{4.8}F_{0.7}$ cathode exhibited facile Na migration despite the micrometer-sized particles. Possible structural defects in the bulk $Na_xVPO_{4.8}F_{0.7}$ hardly obstructed Na migration because Na^+ ions could bypass them easily via the two-dimensional diffusional pathways. The high power electrode with micrometer-sized particles that does not require nanosizing would be beneficial in compensating for a generally low volumetric energy density of polyanion-based electrode materials.

4. DISCUSSION

The charge/discharge mechanism of the $Na_{1.5}VPO_{4.8}F_{0.7}$ cathode is worth describing in greater detail. Despite the apparent two-phase reaction in the electrochemical profile, evidence of the second phase in the ex situ XRD data was not as clear. It is because two end-members of the region have different Na configurations in the basic units on the *ab* plane and do not involve significant structural change. We recall that phases 1, 2, and 3 have different Na-vacancy orderings in the same framework (Figure 2b, inset). Although the Na-vacancy ordering within basic units was relatively strong, interaction among the basic units was weak, as revealed from the first-principle calculations. This situation may easily allow disorder in the long-range Na-vacancy ordering at ambient temperature keeping the short-range ordering in the basic units. Local segregation of two different Na configurations in the material can result in a relatively clear electrochemical footprint of a two-phase reaction, although XRD may be insensitive to it.[8] The continuous lattice parameter change in the two-phase

regions ($1.5 \geq x \geq 1.0$; Figure 3c) could be a consequence of the combination of the coherent interface and the lack of the long-range Na-vacancy ordering, which may result in mosaic-type phase distribution. First, if coherent interfaces between the two phases are present, gradual lattice variation may occur near the interface due to lattice strain. According to a general alloy theory, the coherent interface can be stable at levels below a lattice mismatch between two phases of ~5%.[54] The critical lattice mismatch for incoherent interfaces has also been shown to be ~5% for the olivine $LiMPO_4$ (M = Fe, Mn, and/or Co).[55,56] In our $Na_xVPO_{4.8}F_{0.7}$ system, the lattice misfits in regions I and II were less than 2%, implying the possibility of fully coherent interfaces. Second, when the two phases exist as a mosaic type with an extremely small domain size due to weak long-range interactions, the effect of the coherent interface cannot be neglected. Gradual lattice variation in the interface will significantly affect the overall lattice parameter, eventually leading to continuous lattice parameter change.

Closer examination of the XRD data revealed a hint of a two-phase reaction in the high-voltage region, also evident from the ex situ XRD data in Supporting Information Figure S3. Peak splitting for (220) reflection was clearly observed in this region, particularly during discharge (Supporting Information Figure S3e). These results indicate that local segregation of two Na configurations (i.e., the occurrence of biphasic domains) also occurred in the high-voltage region, although it was much weaker. Interestingly, in the XRD evolution, all reflections except for the (002) and (220) families showed no trace of peak splitting; instead, they continuously shifted throughout the whole region. This phenomenon can be understood by the opposite trends of changes in the *a* and *c* lattice parameters. Because of the canceling of the reduction and increase, much less change in lattice spacing such as d_{222} and d_{113} was observed as compared to d_{220} and d_{002} with indices of *hk*0 or 00*l* (Supporting Information Figure S10). Except for *hk*0 or 00*l*, the Δd_{hkl} is so small that clear resolution with XRD is likely to be difficult. Similarly, the ambiguous biphasic behavior in the high-voltage region is speculated to originate from: (i) (220) and (113) reflections becoming very close in the highly charged state of the material, and (ii) the broad nature of the (002) reflection of phase 3 (i.e., the fully charged phase), which likely obscured the peak splitting.

Finally, it is noteworthy that an abnormally low E_a value was observed, despite the high oxidation states of vanadium (i.e., +4 and +5) in the Na-deficient $Na_xVPO_{5-\delta}F_{0.5+\delta}$ phases. NEB calculations for Na diffusion kinetics in $Na_xVPO_5F_{0.5}$ ($0.5 \leq x \leq 1.5$) revealed that Na^+ ions can move very quickly, regardless of the state of charge. This finding contrasts sharply with the large activation barriers for Li motion (~490 meV) in some layered oxides in highly charged states.[57] In the intermediate state of Li hopping, Li^+ gets too close to the high-valent transition-metal ions (i.e., Co^{4+}, Ni^{4+}, and Mn^{4+}), with large electrostatic repulsion leading to a high activation barrier.[57] However, the Na^+-V^{n+} distance in $Na_xVPO_5F_{0.5}$ does not shorten, even in the intermediate state of path 2, over the trajectory of Na hopping; rather, it increases, as evidenced from NEB calculations (Supporting Information Figure S11). Because the stability of the intermediate state during ion hopping is greatly influenced by the electrostatic repulsion between cations, less Na^+-V^{n+} repulsion during Na migration is expected to lower the activation barrier.

5. CONCLUSION

In summary, a new $Na_{1.5}VPO_{4.8}F_{0.7}$ cathode showed outstanding electrochemical performance for rechargeable sodium batteries. It exhibited a high voltage of ~3.8 V (vs Na^+/Na), giving a large theoretical energy density of ~600 Wh kg^{-1}. The cycling of the material was exceptionally stable as compared to other cathodes for NIBs, which was attributed to the low volume change during cycling. The open framework of $Na_{1.5}VPO_{4.8}F_{0.7}$ allowed fast conduction of Na^+ ions through two-dimensional diffusional pathways, which resulted in excellent rate capability. We believe that our study of this novel $Na_{1.5}VPO_{4.8}F_{0.7}$ cathode with fascinating electrochemical properties can provoke stimulating discussions about the next-generation NIB and its potential new applications.

■ ASSOCIATED CONTENT

Supporting Information

Comparative analysis on ^{31}P MAS NMR data; experimental and simulated XRD patterns of $Na_xVPO_{5-\delta}F_{0.5+\delta}$ (x = 1.5 and 1.0); experimental and simulated XRD patterns of $Na_{1.5}VPO_{4.8}F_{0.7}$ and $Na_{1.0}VPO_{4.8}F_{0.7}$ powders; complete ex situ XRD data of $Na_xVPO_{4.8}F_{0.7}$ electrodes; XRD patterns of pristine and multicycled $Na_{1.5}VPO_{4.8}F_{0.7}$ electrodes; capacity recovery graph; GITT curve; EIS spectra of $Na_{1.5}VPO_{4.8}F_{0.7}$ and $Na_{1.0}VPO_{4.8}F_{0.7}$ pellets for various temperatures and the fitting details; in situ EIS measurement of the $Na_{1.5}VPO_{4.8}F_{0.7}$ electrode during a charge process in GITT mode; activation barrier curves for Na hopping for path 2 in $Na_xVPO_5F_{0.5}$ ($x \approx$ 1.5 and 0.5) from the NEB calculations; changes in calculated *d*-spacing of $Na_xVPO_5F_{0.5}$ with decreasing Na content; and detailed results of NEB calculations. This material is available free of charge via the Internet at http://pubs.acs.org.

■ AUTHOR INFORMATION

Corresponding Author

matlgen1@snu.ac.kr

Author Contributions

⊥These authors contributed equally.

Notes

The authors declare no competing financial interest.

■ ACKNOWLEDGMENTS

This work was supported by (i) the Human Resources Development program (20124010203320) and (ii) the Energy Efficiency & Resources (20112010100140) of the Korea Institute of Energy Technology Evaluation and Planning (KETEP) grant and (iii) the World Premier Materials grant funded by the Korea government Ministry of Trade, Industry and Energy. This work was supported by (iv) the Supercomputing Center/Korea Institute of Science and Technology Information with supercomputing resources including technical support (KSC-2012-C2-78), (v) the Research Center Program of IBS (Institute for Basic Science) in Korea, and (vi) NRF (National Research Foundation of Korea) Grant funded by the Korean Government (NRF-2011-Global Ph.D. Fellowship Program).

■ REFERENCES

(1) Yabuuchi, N.; Kajiyama, M.; Iwatate, J.; Nishikawa, H.; Hitomi, S.; Okuyama, R.; Usui, R.; Yamada, Y.; Komaba, S. *Nat. Mater.* **2012**, *11*, 512.

(2) Jian, Z.; Han, W.; Lu, X.; Yang, H.; Hu, Y.-S.; Zhou, J.; Zhou, Z.; Li, J.; Chen, W.; Chen, D.; Chen, L. *Adv. Energy Mater.* **2013**, *3*, 156.
(3) Ponrouch, A.; Marchante, E.; Courty, M.; Tarascon, J.-M.; Palacin, M. R. *Energy Environ. Sci.* **2012**, *5*, 8572.
(4) Kim, S.-W.; Seo, D.-H.; Ma, X.; Ceder, G.; Kang, K. *Adv. Energy Mater.* **2012**, *2*, 710.
(5) Ellis, B. L.; Nazar, L. F. *Curr. Opin. Solid State Mater. Sci.* **2012**, *16*, 168.
(6) Palomares, V.; Serras, P.; Villaluenga, I.; Hueso, K. B.; Carretero-Gonzalez, J.; Rojo, T. *Energy Environ. Sci.* **2012**, *5*, 5884.
(7) Pan, H.; Hu, Y.-S.; Chen, L. *Energy Environ. Sci.* **2013**, *6*, 2338.
(8) Berthelot, R.; Carlier, D.; Delmas, C. *Nat. Mater.* **2011**, *10*, 74.
(9) Ding, J. J.; Zhou, Y. N.; Sun, Q.; Yu, X. Q.; Yang, X. Q.; Fu, Z. W. *Electrochim. Acta* **2013**, *87*, 388.
(10) Guignard, M.; Didier, C.; Darriet, J.; Bordet, P.; Elkaïm, E.; Delmas, C. *Nat. Mater.* **2013**, *12*, 74.
(11) Yabuuchi, N.; Yano, M.; Yoshida, H.; Kuze, S.; Komaba, S. *J. Electrochem. Soc.* **2013**, *160*, A3131.
(12) Vassilaras, P.; Ma, X.; Li, X.; Ceder, G. *J. Electrochem. Soc.* **2013**, *160*, A207.
(13) Shakoor, R. A.; Seo, D.-H.; Kim, H.-S.; Park, Y.-U.; Kim, J.; Kim, S.-W.; Gwon, H.; Lee, S.; Kang, K. *J. Mater. Chem.* **2012**, *22*, 20535.
(14) Gover, R. K. B.; Bryan, A.; Burns, P.; Barker, J. *Solid State Ionics* **2006**, *177*, 1495.
(15) Barker, J.; Gover, R. K. B.; Burns, P.; Bryan, A. J. *Electrochem. Solid-State Lett.* **2006**, *9*, A190.
(16) Casas-Cabanas, M.; Roddatis, V. V.; Saurel, D.; Kubiak, P.; Carretero-Gonzalez, J.; Palomares, V.; Serras, P.; Rojo, T. *J. Mater. Chem.* **2012**, *22*, 17421.
(17) Moreau, P.; Guyomard, D.; Gaubicher, J.; Boucher, F. *Chem. Mater.* **2010**, *22*, 4126.
(18) Kim, H.; Shakoor, R. A.; Park, C.; Lim, S. Y.; Kim, J.-S.; Jo, Y. N.; Cho, W.; Miyasaka, K.; Kahraman, R.; Jung, Y.; Choi, J. W. *Adv. Funct. Mater.* **2013**, *23*, 1147.
(19) Barpanda, P.; Ye, T.; Nishimura, S.-i.; Chung, S.-C.; Yamada, Y.; Okubo, M.; Zhou, H.; Yamada, A. *Electrochem. Commun.* **2012**, *24*, 116.
(20) Oh, S.-M.; Myung, S.-T.; Hassoun, J.; Scrosati, B.; Sun, Y.-K. *Electrochem. Commun.* **2012**, *22*, 149.
(21) Sauvage, F.; Quarez, E.; Tarascon, J.-M.; Baudrin, E. *Solid State Sci.* **2006**, *8*, 1215.
(22) Kawabe, Y.; Yabuuchi, N.; Kajiyama, M.; Fukuhara, N.; Inamasu, T.; Okuyama, R.; Nakai, I.; Komaba, S. *Electrochem. Commun.* **2011**, *13*, 1225.
(23) Saravanan, K.; Mason, C. W.; Rudola, A.; Wong, K. H.; Balaya, P. *Adv. Energy Mater.* **2013**, *3*, 444.
(24) Ellis, B. L.; Makahnouk, W. R. M.; Rowan-Weetaluktuk, W. N.; Ryan, D. H.; Nazar, L. F. *Chem. Mater.* **2009**, *22*, 1059.
(25) Sakaushi, K.; Hosono, E.; Nickerl, G.; Gemming, T.; Zhou, H.; Kaskel, S.; Eckert, J. *Nat. Commun.* **2013**, *4*, 1485.
(26) Sakaushi, K.; Nickerl, G.; Wisser, F. M.; Nishio-Hamane, D.; Hosono, E.; Zhou, H.; Kaskel, S.; Eckert, J. *Angew. Chem., Int. Ed.* **2012**, *51*, 7850.
(27) Park, Y.-U.; Seo, D.-H.; Kim, B.; Hong, K.-P.; Kim, H.; Lee, S.; Shakoor, R. A.; Miyasaka, K.; Tarascon, J.-M.; Kang, K. *Sci. Rep.* **2012**, *2*, 704.
(28) Roisnel, T.; Rodríquez-Carvajal, J. *Materials Science Forum*; Transtec Publications: Germany, 1999, 2001; Vol. *378*, p 118.
(29) Perdew, J. P.; Burke, K.; Ernzerhof, M. *Phys. Rev. Lett.* **1996**, *77*, 3865.
(30) Kresse, G.; Furthmüller, J. *Comput. Mater. Sci.* **1996**, *6*, 15.
(31) Anisimov, V. I.; Zaanen, J.; Andersen, O. K. *Phys. Rev. B* **1991**, *44*, 943.
(32) Van der Ven, A.; Thomas, J. C.; Xu, Q.; Bhattacharya, J. *Math. Comput. Simulat.* **2010**, *80*, 1393.
(33) Van der Ven, A.; Thomas, J. C.; Xu, Q.; Swoboda, B.; Morgan, D. *Phys. Rev. B* **2008**, *78*, 104306.
(34) Toukmaji, A. Y.; Board, J. A., Jr. *Comput. Phys. Commun.* **1996**, *95*, 73.
(35) Henkelman, G.; Uberuaga, B. P.; Jónsson, H. *J. Chem. Phys.* **2000**, *113*, 9901.
(36) Sale, M.; Avdeev, M. *J. Appl. Crystallogr.* **2012**, *45*, 1054.
(37) Momma, K.; Izumi, F. *J. Appl. Crystallogr.* **2008**, *41*, 653.
(38) Grey, C. P.; Dupré, N. *Chem. Rev.* **2004**, *104*, 4493.
(39) Carlier, D.; Ménétrier, M.; Grey, C. P.; Delmas, C.; Ceder, G. *Phys. Rev. B* **2003**, *67*, 174103.
(40) Meng, Y. S.; Hinuma, Y.; Ceder, G. *J. Chem. Phys.* **2008**, *128*, 104708.
(41) Melot, B. C.; Tarascon, J. M. *Acc. Chem. Res.* **2013**, *46*, 1226.
(42) Wong, J.; Lytle, F. W.; Messmer, R. P.; Maylotte, D. H. *Phys. Rev. B* **1984**, *30*, 5596.
(43) Yoon, J.; Muhammad, S.; Jang, D.; Sivakumar, N.; Kim, J.; Jang, W.-H.; Lee, Y.-S.; Park, Y.-U.; Kang, K.; Yoon, W.-S. *J. Alloys Compd.* **2013**, *569*, 76.
(44) Kim, H.; Park, I.; Seo, D.-H.; Lee, S.; Kim, S.-W.; Kwon, W. J.; Park, Y.-U.; Kim, C. S.; Jeon, S.; Kang, K. *J. Am. Chem. Soc.* **2012**, *134*, 10369.
(45) Sun, Y.; Zhao, L.; Pan, H.; Lu, X.; Gu, L.; Hu, Y.-S.; Li, H.; Armand, M.; Ikuhara, Y.; Chen, L.; Huang, X. *Nat. Commun.* **2013**, *4*, 1870.
(46) Wang, L.; Lu, Y.; Liu, J.; Xu, M.; Cheng, J.; Zhang, D.; Goodenough, J. B. *Angew. Chem., Int. Ed.* **2013**, *52*, 1964.
(47) Delacourt, C.; Laffont, L.; Bouchet, R.; Wurm, C.; Leriche, J.-B.; Morcrette, M.; Tarascon, J.-M.; Masquelier, C. *J. Electrochem. Soc.* **2005**, *152*, A913.
(48) Recham, N.; Chotard, J. N.; Dupont, L.; Delacourt, C.; Walker, W.; Armand, M.; Tarascon, J. M. *Nat. Mater.* **2010**, *9*, 68.
(49) Sadaoka, Y.; Matsuguchi, M.; Sakai, Y.; Nakayama, S. *J. Mater. Sci.* **1989**, *24*, 1299.
(50) Bohnke, O.; Ronchetti, S.; Mazza, D. *Solid State Ionics* **1999**, *122*, 127.
(51) Chen, C. H.; Vaughey, J. T.; Jansen, A. N.; Dees, D. W.; Kahaian, A. J.; Goacher, T.; Thackeray, M. M. *J. Electrochem. Soc.* **2001**, *148*, A102.
(52) Kang, K.; Ceder, G. *Phys. Rev. B* **2006**, *74*, 094105.
(53) Malik, R.; Burch, D.; Bazant, M.; Ceder, G. *Nano Lett.* **2010**, *10*, 4123.
(54) Porter, D. A.; Easterling, K. E. *Phase Transformations in Metals and Alloys*; CRC Press: New York, 1992.
(55) Park, K.-Y.; Hong, J.; Kim, J.; Park, Y.-U.; Kim, H.; Seo, D.-H.; Kim, S.-W.; Choi, J.-W.; Kang, K. *J. Electrochem. Soc.* **2013**, *160*, A444.
(56) Tang, M.; Belak, J. F.; Dorr, M. R. *J. Phys. Chem. C* **2011**, *115*, 4922.
(57) Kang, K.; Meng, Y. S.; Bréger, J.; Grey, C. P.; Ceder, G. *Science* **2006**, *311*, 977.